

- L.), D. Reidel Publishing Co, Dordrecht, The Netherlands, 1973, pp. 347–361.
4. Horanyi, M., Charged dust dynamics in the solar system. *Annu. Rev. Astron. Astrophys.*, 1996, **34**, 383–418.
 5. Criswell, D. R., Lunar dust motion. In Proceedings of the Third Lunar Science Conference, Houston, Texas, 1972, vol. 3, pp. 2671–2680.
 6. Delory, G. T., Electrical phenomena on the Moon and Mars. Proceedings of the ESA Annual Meeting on Electrostatics, University of North Carolina, Charlotte, 2010, Paper A1.
 7. Berg, O. E., Wolf, H. and Rhee, J., Lunar soil movement registered by the Apollo 17 cosmic dust experiment. In *Interplanetary Dust and Zodiacal Light* (eds Elsasser, H. and Fechtig, H.), Springer-Verlag, Berlin, 1976, pp. 233–237.
 8. Stubbs, T. J., Vondrak, R. R. and Farrell, W. M., A dynamic fountain model for lunar dust. *Adv. Space Res.*, 2006, **37**, 59–66.
 9. McCoy, J. E., Photometric studies of light scattering above the lunar terminator from Apollo solar corona photography. *Lunar Planet Sci. Conf.*, 1976, 1087–1112.
 10. Murphy, D. L. and Vondrak, R. R., Effects of levitated dust on astronomical observations from the lunar surface. *Lunar Planet Sci. Conf.*, 1993, 1033–1034.
 11. Zvereva, A. M., Severnyi, A. B. and Terez, E. I., The measurements of sky brightness on Lunokhod-2. *Moon*, 1975, **14**, 123–128.
 12. Zook, H. A., Potter, A. E. and Cooper, B. L., The lunar dust exosphere and Clementine lunar horizon glow. *Lunar Planet Sci. Conf.*, 1995, **26**, 1577.
 13. Grun, E., Horanyi, M. and Sternovsky, Z., The lunar dust environment. *Planet. Space Sci.*, 2011, **59**, 1672–1680.
 14. Stubbs, T. J., Glenar, D. A., Farrell, W. M., Vondrak, R. R., Collier, M. R., Halekas, J. S. and Delory, G. T., On the role of dust in the lunar ionosphere. *Planet. Space Sci.*, 2011, **59**, 1659–1664.
 15. Glenar, D. A., Stubbs, T. J., McCoy, J. E. and Vondrak, R. R., A reanalysis of the Apollo light scattering observations and implications for lunar exospheric dust. *Planet. Space Sci.*, 2011, **59**, 1695–1707.
 16. Pines, V., Zlatkowski, M. and Chait, A., Lofted charged dust distribution above the Moon surface. *Planet. Space Sci.*, 2011, **59**, 1795–1803.
 17. Horanyi, M. *et al.*, The dust environment of the Moon as seen by the Lunar Dust Experiment (LDEX). In 45th Lunar and Planetary Science Conference, The Woodlands, Texas, 2014, abstract #1303.
 18. Horanyi, M., Szalay, J. R., Kempf, S., Schmidt, J., Grun, E., Srama, R. and Sternovsky, Z., A permanent, asymmetric dust cloud around the Moon. *Nature*, 2015, **522**, 324–326.
 19. Whipple, E. C., Potentials of surfaces in space. *Rep. Prog. Phys.*, 1981, **44**, 1197–1250.
 20. Goertz, C. K., Dusty plasmas in the solar system. *Rev. Geophys.*, 1989, **27**(2), 271–292.
 21. http://en.wikipedia.org/wiki/Debye_length (accessed on 29 October 2014).
 22. Heiken, G. H., Vaniman, D. T. and French, B. M., *Lunar Source Book*, Cambridge University Press, 1991.
 23. Colwell, J. E., Gulbis, A. A. S., Horanyi, M. and Robertson, S., Dust transport in photoelectron layers and the formation of dust ponds on Eros. *Icarus*, 2005, **175**(1), 159–169.
 24. Rhee, J. W., Berg, O. E. and Wolf, H., *Electrostatic Dust Transport and Apollo 17 LEAM Experiment*, COSPAR Space Research XVII, Pergamon, New York, 1977, pp. 627–629.
 25. Hundhausen, A. J., The solar wind. In *Introduction to Space Physics*, (eds Kivelson, M. G. and Russell, C. T.), Cambridge University Press, 1995.
 26. Slavin, J. A., Smith, E. J., Sibeck, D. G., Baker, D. N., Zwicki, R. D. and Akasofu, S. I., An ISEE 3 study of average and substorm conditions in the distant magnetotail. *J. Geophys. Res.*, 1985, **90**(A11), 10875–10895.
 27. Larson, D. E., Lin, R. P. and Steinberg, J., Extremely cold electrons in the January 1997 magnetic cloud. *Geophys. Res. Lett.*, 2000, **27**(2), 157–160.
 28. Halekas, J. S., Delory, G. T., Lin, R. P., Stubbs, T. J. and Farrell, W. M., Lunar prospector observations of the electrostatic potential of the lunar surface and its response to incident currents. *J. Geophys. Res.*, 2008, **113**, A09102.
 29. Pabari, J. P. *et al.*, Moon Electrostatic Potential and Dust Analyser (MESDA) for future lunar mission. In 46th Lunar and Planetary Science Conference, The Woodlands, Texas, 16–20 March 2015, abstr. #1167.

ACKNOWLEDGEMENTS. We thank the anonymous reviewer for constructive comments that helped improve the manuscript and Prof. A. K. Singal, Physical Research Laboratory, India for useful suggestions.

Received 22 June 2015; revised accepted 9 December 2015

doi: 10.18520/cs/v110/i10/1984-1989

Photonic crystal-based force sensor to measure sub-micro newton forces over a wide range

T. Sreenivasulu^{1,*}, Venkateswara Rao Kolli¹,
T. R. Yadunath¹, T. Badrinarayana¹,
Amaresh Sahu¹, Gopalkrishna Hegde², S. Mohan²
and T. Srinivas¹

¹Department of Electrical Communication Engineering, and

²Centre for Nano Science and Engineering, Indian Institute of Science, Bengaluru 560 012, India

A photonic crystal-based force sensor to measure forces in the wide range 100 nN–10 μN is proposed here. An optimized photonic crystal resonator integrated on top of a Si/SiO₂ bilayer cantilever, is used as the sensing device. A sensitivity of 0.1 nm for a force of 100 nN is obtained with a high-quality factor of 10,000. The sensor characteristics in the force ranges 0–1 μN and 0–10 μN are also presented here. Linear wavelength shift and constant quality factor are observed in the entire studied force range.

Keywords: Cantilever beam, force sensing, optical sensors, photonic crystal resonator.

PHOTONIC crystals (PhC) are artificial materials in which refractive index varies periodically. If these refractive indices are sufficiently different, it will give rise to photonic bandgap, which causes prevention of light propagation within a specified range of frequencies spanned by the bandgap. It is possible to manipulate the flow of light within PhCs¹, which makes them promising

*For correspondence. (e-mail: sulupinky@ece.iisc.ernet.in)

devices for different applications in several fields. Important applications of PhC include PhC lasers², demultiplexers in WDM systems³, slow light devices⁴, chemical sensing⁵, bio-sensing⁶, humidity sensing⁷, temperature sensing⁸ and pressure sensing⁹.

Apart from the above-mentioned sensing applications, force sensing by PhC devices attracted attention as the PhC structures are extremely sensitive to mechanical deformation. In these devices the principle of operation is the elasto-optic effect, in which refractive index variation is induced by mechanical stress. The PhC devices embedded on the surface of a microcantilever are of interest, as PhC are extremely sensitive to mechanical bending deformation of the surface of the cantilever beam. Most of the commercially available cantilever deflection sensors consist of an external laser diode unit and a photodiode reported¹⁰. Various MEMS-based cantilever deflection sensors using sensing mechanisms such as piezoresistive scheme¹¹, piezoelectric scheme¹² and capacitive scheme¹³ have been reported. Cantilevers integrated with PhC are extremely small in size and highly sensitive compared to the above-mentioned devices. Most importantly, these devices can be integrated with other photonic devices. Several PhC-based force sensors based on external mechanical tuning are reported, in which the PhC device is integrated on top of a cantilever. An ultrasensitive pressure and force sensor is proposed, in which dual-layered InGaAsP PhC micro cavity is used as the sensing element¹⁴. In this device, multiple beams integrated with PhCs are cascaded to enhance the sensitivity of the device. Later, efforts are made to design single cantilever beam sensors with PhC integration. A PhC nano-cavity resonator on top of a 220 nm thick silicon cantilever beam is proposed¹⁵. The obtained minimum detectable force is 62.5 nN for a wavelength resolution of 0.1 nm. On the other hand, a Si/SiO₂ bilayer cantilever with PhC ring resonator on top is reported¹⁶. A sensitivity of 0.1 nm/76 nN with an average quality factor (Q) of 3470 is obtained. Li *et al.*^{17,18} presented a more sensitive device which consists of a dual PhC ring resonator on a 220 nm thick silicon cantilever. Among different configurations of sensors that are reported in these contributions, the most sensitive device has a minimum detectable force as 7.58 nN, but with a drastically reduced Q of 876. Apart from these devices, a shoulder-coupled aslant nano-cavity-based PC stress sensor is proposed, which is capable of sensing in two directions¹⁹. In horizontal and vertical directions, the sensitivity is found to be 7.5 and 10 nm/ μ N respectively, with a Q factor of 3000.

In most of the above-mentioned applications, good quality factor is essential to ensure optimal performance. In particular, for force sensing application, Q should be as high as possible and it should be constant for all the measured forces. In this work, we designed a PhC ring resonator-based force sensor with high Q factor, linear wavelength shift and almost constant normalized inten-

sity. The design and modelling involves two phases. In the first phase, the PhC ring resonator is optimized to show high quality factor. This is done by several iterations of finite difference time domain (FDTD) method simulations to obtain the transmission spectrum of the device. In the second phase, finite element method (FEM) simulations are performed to obtain the deformation of PhC structure under various applied forces. These deformations are applied in FDTD simulations to obtain the sensor characteristics for various applied forces. The proposed device is studied under applied forces of a wide range from 0 to 10 μ N. In the following we deal with design of an optical device with 2D FDTD simulations and then explain the force sensing characteristics with simultaneous FEM and FDTD simulations. Conclusions are given at the end.

The PhC device consists of a hexagonal lattice of air holes on a 220 nm thick silicon device layer, which is integrated with a 600 nm thick SiO₂ layer underneath (Figure 1). Thus, the device comprises three layers of different materials, namely air/Si-220 nm thick/SiO₂-600 nm thick with refractive indices of 1/3.46/1.45 respectively. All these dimensions are considered based on the existing silicon process technology. The effective refractive index is derived as 2.82. The lattice constant and hole radius of PhC device are taken as 410 and 120 nm respectively. Defects are added into the PhC structure, so that line defect waveguides and hexagonal ring are formed in the structure. This is done by removing two rows of holes and removing holes along the contour of the hexagonal ring (Figure 1). As shown in Figure 1, there are four port in the PhC device, namely input port, transmission port, forward drop port and backward drop port. A broadband source of light centred at wavelength of 1550 nm is chosen as the input at the input port. According to the design of the sensor, our signal of interest is backward drop based on which the force is sensed.

In 2D FDTD simulations, the effective refractive index of 2.82 is used to get transmission spectra at various ports (Figure 2). Two peaks can be noticed in the backward drop spectrum at 1553 and 1562 nm. Since the peak at 1562 nm is relatively sharper with a quality factor of around 3000, we consider this peak as the output of the sensor. This configuration of PhC ring resonator with Si/SiO₂ cantilever will not serve the purpose of force sensing properly, as it is observed that the Q and normalized intensity vary significantly as the applied force increases. To avoid this issue, we optimized the PhC ring resonator such that Q is improved further and is constant for all applied forces. This involves optimizing the size of holes inside the hexagonal ring, where the radius of the centre hole inside the ring is denoted by R_0 , and the size of the holes in the succeeding rings is denoted by R_1 and R_2 respectively. As these holes with optimized radii are sufficiently separated from the line defect waveguides, it does not affect the quality factor; even when

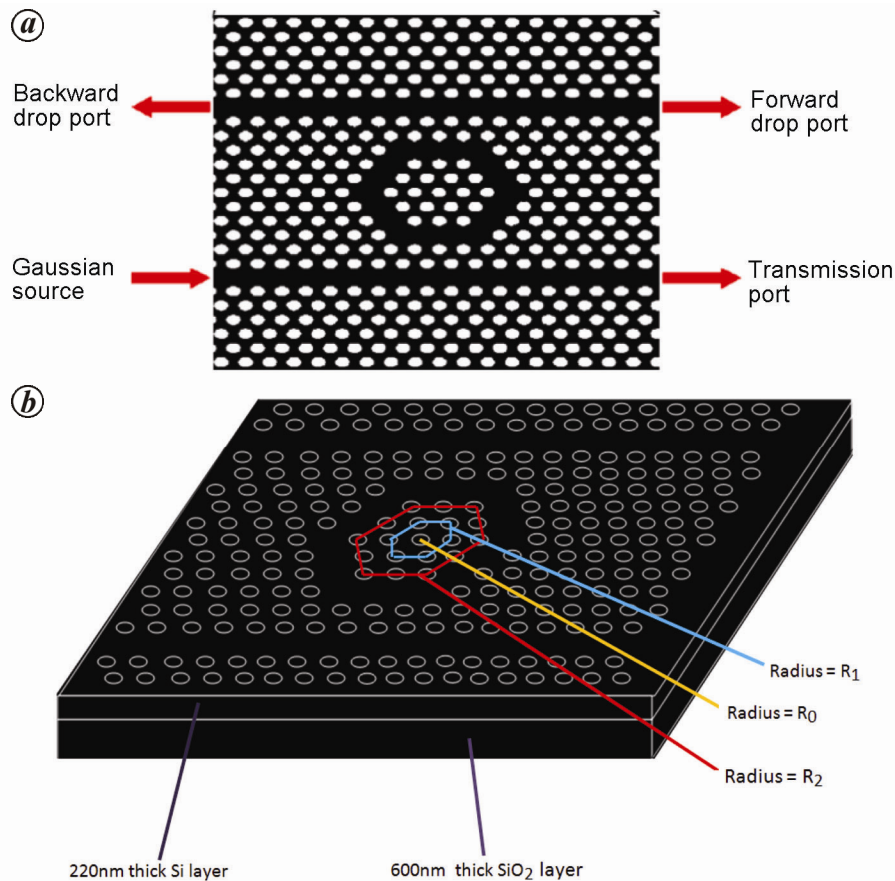


Figure 1. *a*, Top view of photonic crystal (PhC) ring resonator. *b*, 3D schematic of the PhC ring resonator.

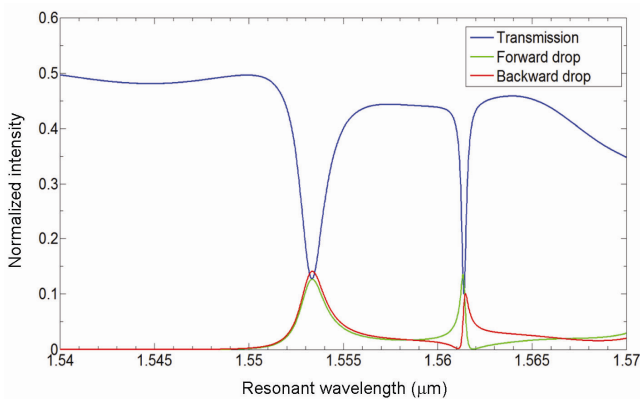


Figure 2. Transmission spectra at various ports of PhC ring resonator.

deformation occurs because of the applied force, Q remains the same.

Quality factor of any PhC device can be increased by increasing the size of the cavity. In our work, we have chosen the central hole with radius R_0 inside the hexagonal ring as the cavity. Significant improvement in Q is observed with increase in R_0 . During this process of increasing R_0 fabrication limitations are considered. According to these limitations, there should be at least

100 nm of separation between successive holes. Hence R_0 is optimized to 140 nm to keep the separation between holes above 100 nm. It is observed that if R_0 alone is increased, the cavity becomes more multimodal. To avoid this, we reduce the refractive index contrast by optimizing R_1 and R_2 as well, so that the values of R_0 , R_1 and R_2 are close. The optimized values of R_0 , R_1 and R_2 are 140, 135 and 130 nm respectively. Figure 3 shows the transmission spectra at various ports of the PhC device with optimized R_0 , R_1 and R_2 . It can be noticed that the Q factor is increased to 10,000 at wavelength 1552 nm, shown in red colour. Because of increased Q , this PhC device can be used as a force sensor over a wide range of forces. Next we deal with force sensor characteristics.

The proposed force sensor consists of a bilayer cantilever with 220 nm silicon layer integrated on a 600 nm silicon dioxide layer. The 220 nm thick Si layer acts as device layer. The optimized PhC ring resonator is made on this device layer, in such a way that the ring resonator will be affected by maximum applied stress leading to more strain in the longitudinal direction. Here strain is considered as percentage change in the diameter (D) of the hexagonal ring. Three-fourth of the PhC device is kept on the cantilever beam and ring is placed at the junction of the beam and bulk part of the cantilever, as shown

in Figure 4. As mentioned earlier, the principle of operation of the device is based on elasto-optic effect. When force is applied in the Z-direction on the tip of the cantilever, the air holes will be displaced in the direction parallel to the line defect waveguides. Thus, the hexagonal ring will be elongated in the longitudinal direction, changing the ring to become more oval-shaped. This deformation of the ring will cause resonant wavelength shift towards longer wavelength. In order to obtain the deformation data corresponding to various applied forces, FEM simulations are performed. For each applied force, the corresponding resonant wavelength is obtained by performing FDTD method simulations over the deformed PhC structure.

In FEM simulations the Young's modulus and Poisson's ratio of Si and SiO₂ are chosen as 130 GPa, 70 GPa and 0.3, 0.17 respectively. Along with the above-mentioned parameters, the refractive index of silicon

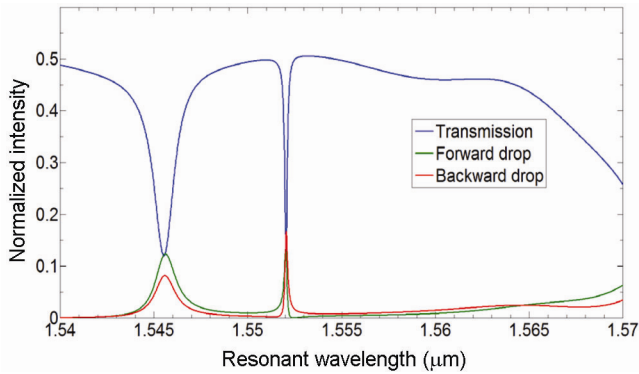


Figure 3. Transmission at various ports of optimized PhC ring resonator.

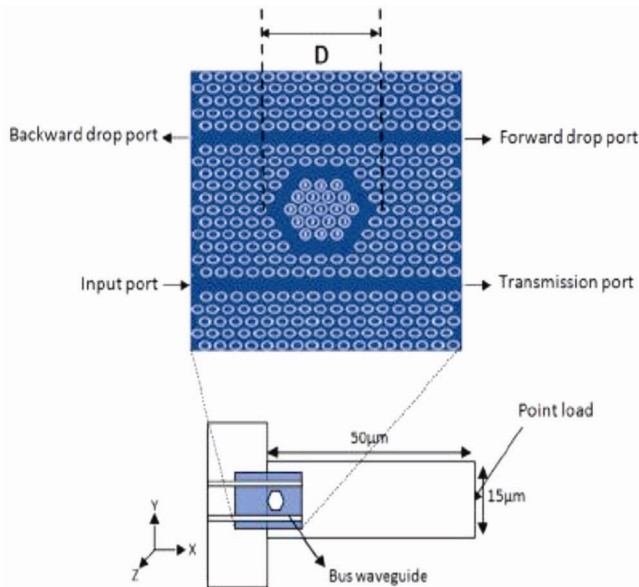


Figure 4. Schematic of the PhC ring resonator-based force sensor integrated on top of Si/SiO₂ cantilever.

remains unaffected at room temperature. Hence the temperature effects on the device at room-temperature are not considered. Simulations are performed for forces in the ranges 0–1 μN and 0–10 μN, with force increment of 0.1 and 1 μN respectively. Figure 5 shows the positions of various peaks corresponding to different applied forces in the range 0–1 μN. It can be seen from the figure that the peak intensities and Q factors are uniform and the wavelength shift is linear with respect to applied force. Similar behaviour of these parameters can be observed in the device characteristics for the forces in the range 0–10 μN as well (Figure 6). From these characteristics, the sensitivity of the device is derived as 10 nm for an applied force of 10 μN. Almost the same sensitivity is observed in the force range 0–1 μN as well. The results obtained are compared with those of planar nano-ring resonator (NRR)-based sensor reported by Mai *et al.*¹⁶ (Table 1). Even though the proposed sensor offers less sensitivity than the one reported, because of the optimized ring resonator structure and increased Q factor, the ability to measure the sub-micro Newton forces is improved. Hence forces over a wide range can be detected with minimum variation of Q factor, as shown in Table 1. In the earlier

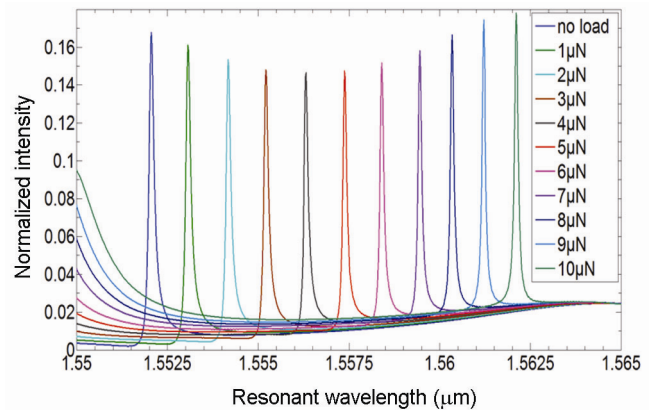


Figure 5. Variation of resonant wavelength with respect to applied force in the range 0–10 μN.

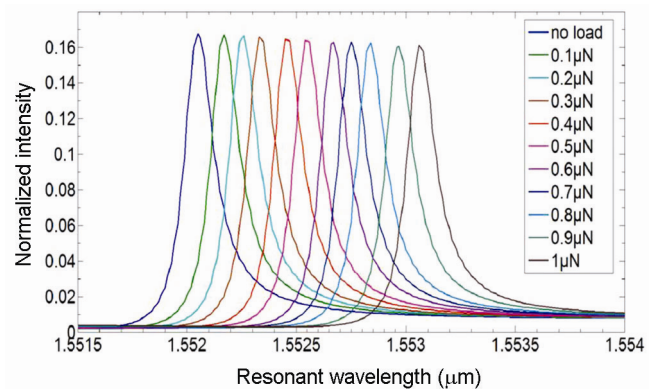
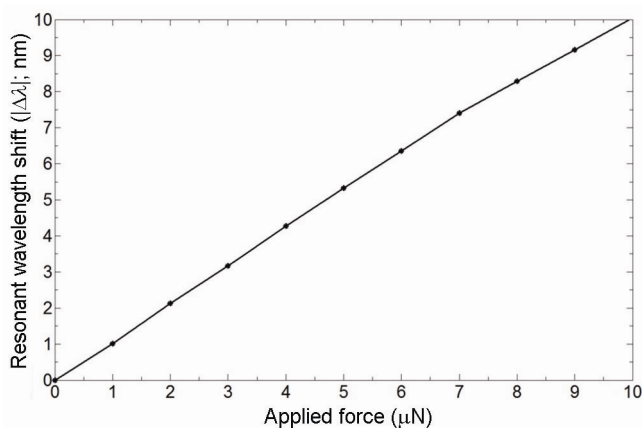


Figure 6. Variation of resonant wavelength with respect to applied force in the range 0–1 μN.

Table 1. Performance comparison of the proposed force sensor and that reported in the literature

Results of NRR-based sensor proposed by Mai <i>et al.</i> ¹⁶		Results of optimized ring resonator-based sensor proposed in the present study	
Force (μN)	Q factor	Force (μN)	Q factor
0	3897	0	10000
5	3509	5	10010
7.5	2962	7.5	10152
10	3520	10	9951
Reported sensitivity is 0.1 nm for an applied force of 76 nN		The obtained sensitivity is 0.1 nm for an applied force of 100 nN	

**Figure 7.** Variation of resonant wavelength shift with respect to applied force in the studied force range.

work, resonant wavelength peaks for all applied forces were not readable; however, they are readable only for those forces that are presented in Table 1. Based on these observations, it can be noticed that the present sensor will give better performance compared to the one reported. Our simulation results have shown that the detection capability with high Q factor can be continued up to 18 μN of the applied force. When forces beyond 18 μN are applied, because of the abnormal variation of refractive index on the surface of the cantilever beam, the wavelength shift may not be linear, leading to Q factor degradation.

Thus, the proposed sensor can measure very small forces in a wide range from 100 nN to 10 μN with linear wavelength shift (Figure 7) and constant Q factor. Since the sensor is highly sensitive, the microcantilever surface can be functionalized to bio-applications like detecting DNA, protein molecules, etc.

In this work, a PhC ring resonator-based force sensor which is capable of sensing forces in a wide range, i.e. 0–10 μN is proposed. The PhC ring resonator is optimized to get high Q factor of 10,000 and it is observed that Q remains the same throughout the studied force range. Force sensor characteristics of the sensor in the ranges 0–1 μN and 0–10 μN are presented. From these results, it can be concluded that the device is capable of measuring

forces in the specified wide range with high Q factor and linear wavelength shift. The designed sensor may find potential applications in bio-sensing like detecting DNA, proteins, etc.

1. Johnson, S. G., Fan, S., Villeneuve, P. R., Joannopoulos, J. D. and Kolodziejcki, L. A., Guided modes in photonic crystal slabs. *Phys. Rev. B*, 1999, **60**, 5751.
2. Hatice Altug, Englund, D. and Jelena Vučković, Ultrafast photonic crystal nano cavity array laser. *Optics Express*, 2006, **13**(22), 8819.
3. Zetao Ma and Kazuhiko Ogasu, Channel drop filters using photonic crystal Fabry–Perot resonators. *Opt. Commun.*, 2011, **284**, 1192–1196.
4. Mulot, M., Saynatjoki, A., Arpiainen, S., Lipsanen, H. and Aho-pelto, J., Slow light propagation in photonic crystal waveguides with ring-shaped holes. *J. Opt A: Pure Appl. Opt.*, 2007, **9**, S415–S418.
5. Kangtaek Lee and Sanford A. Asher, Photonic crystal chemical sensors: pH and ionic strength. *J. Am. Chem. Soc.*, 2000, **122**, 9534–9537.
6. Elewout Hallynck and Peter Bienstman, Photonic crystal biosensor based on angular spectrum analysis. *Opt. Express*, 2010, **18**(17), 18164.
7. Jae Hyun Kim, Jun Hyuk Moon, Seung-Yop Lee and Jungyul Park, Biologically inspired humidity sensor based on three-dimensional photonic crystals. *Appl. Phys. Lett.*, 2010, **97**, 103701.
8. Lu, Y., Wang, M. T., Hao, C. J., Zhao, Z. Q. and Yao, J. Q., Temperature sensing using photonic crystal fiber filled with silver nano wires and liquid. *IEEE Photonics J.*, 2014, **6**(3).
9. Bo Li and Chengkuo Lee, NEMS diaphragm sensors integrated with triple-nano-ring resonator. *Sensors Actuat. A*, 2011, **172**, 61–68.
10. Meyer, G. and Amer, N. M., Novel optical approach to atomic force microscopy. *Appl. Phys. Lett.*, 1988, **53**, 1045–1047.
11. Tortonese, M., Barrett, R. C. and Quate, C. F., Atomic resolution with an atomic force microscope using piezoresistive detection. *Appl. Phys. Lett.*, 1993, **62**, 834–836.
12. Lee, C., Itoh, T., Maeda, R. and Suga, T., Characterization of micromachined piezoelectric PZT force sensors for dynamic scanning force microscopy. *Rev. Sci. Instrum.*, 1997, **68**, 2091–2100.
13. Brugger, J., Buser, R. A. and de Rooij, N. F., Micromachined atomic force microprobe with integrated capacitive readout. *J. Micromech. Microeng.*, 1992, **2**, 218–220.
14. Tsan-Wen Lu and Po-Tsung Lee, Ultra-high sensitivity optical stress sensor based on double layered photonic crystal microcavity. *Opt. Express*, 2009, **17**(3), 1519.
15. Chengkuo Lee and Jayaraj Thillaigovindan, Optical nanomechanical sensor using a silicon photonic crystal cantilever embedded with a nanocavity resonator. *Appl. Opt.* 2009, **48**(10), 1797–1803.

16. Trong Thi Mai, Fu-Li Hsiao, Chengkuo Lee, Wenfeng Xiang, Chii-Chang Chen and Choi, W. K., Optimization and comparison of photonic crystal resonators for silicon microcantilever sensors. *Sensors Actuat. A*, 2011, **165**, 16–25.
17. Li, B., Hsiao, F. L. and Lee, C., Configuration analysis of sensing element for photonic crystal based NEMS cantilever using dual nano-ring resonator. *Sensors Actuator. A: Phys.*, 2011, **169**, 352–361.
18. Li, B., Fu-Li Hsiao and Chengkuo Lee, Computational characterization of a photonic crystal cantilever sensor using a hexagonal dual nano ring based channel drop filter. *IEEE Trans. Nanotechnol.*, 2011, **10**(4).
19. Yi Yang, Daquan Yang, Huiping Tian and Yuefeng Ji, Photonic crystal stress sensor with high sensitivity in double directions based on shoulder-coupled aslant nano cavity. *Sensors Actuat. A*, 2013, **193**, 149–154.

Received 20 October 2015; revised accepted 26 December 2015

doi: 10.18520/cs/v110/i10/1989-1994

Study of relationship between daily maxima in ozone and temperature in an urban site in India

S. S. Gunthe¹, G. Beig² and L. K. Sahu^{3,*}

¹EWRE Division, Department of Civil Engineering, Indian Institute of Technology Madras, Chennai 600 036, India

²Indian Institute of Tropical Meteorology, Pashan, Pune 411 008, India

³Physical Research Laboratory, Navarangpura, Ahmedabad 380 009, India

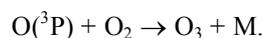
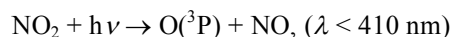
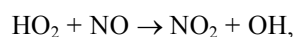
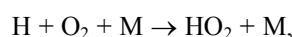
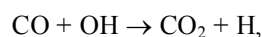
The relationship between surface-level observations of daily maxima in ozone ($O_{3\max}$) volume mixing ratio and ambient air temperature (T_{\max}) has been studied at an urban site, i.e. Pune (18.4°N, 73.8°E), India during 2003–04. The mixing ratios of $O_{3\max}$ were found to be highest during winter to pre-monsoon period and lowest in the monsoon season. The dependence of $O_{3\max}$ levels on T_{\max} has been quantified using the linear regression fit for the different seasons. However, except for the monsoon season, reasonably good correlations between $O_{3\max}$ and T_{\max} were noticed. The correlation between daily $O_{3\max}$ concentration and minimum NO_x ($NO_{x\min}$) concentration was also studied to assess the importance of photochemical mechanism mainly reduction in the loss due to titration. Overall, the strong dependencies of $O_{3\max}$ on T_{\max} and $NO_{x\min}$ signify the role of both meteorological and photochemical processes during most months of a year. The positive slopes of $\Delta O_{3\max}/\Delta T_{\max}$ and $\Delta O_{3\max}/\Delta NO_{x\min}$ clearly indicate the role of significant production and accumulation of O_3 under high temperature and low NO_x conditions respectively, during winter and pre-

monsoon seasons. The statistical analysis of O_3 in relation with the key meteorological and chemical parameters is important to understand the sensitivity of secondary pollutants on various controlling factors.

Keywords: Air temperature, ozone, precursors, seasonal variations.

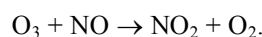
It is well known that surface level ozone (O_3) is one of the important photochemical pollutants due to its strong oxidizing nature. Ozone is produced by the photo-oxidation of precursor gases like volatile organic compounds (VOCs), carbon monoxide (CO) and nitrogen oxides (NO_x ; i.e. $NO + NO_2$) in the presence of sunlight¹. For example, the following set of reactions initiated by the oxidation of CO shows the mechanism of photochemical production of O_3 .

Reaction set 1



The above cycle can be generalized for other precursors like methane (CH_4) and nonmethane hydrocarbons (NMHCs) as well. The production efficiency of O_3 has been observed to depend on several meteorological parameters such as solar radiation flux and temperature. In general, O_3 mixing ratio will increase when incoming solar ultraviolet (UV) flux reaches a maximum, clouds are few and levels of precursors are optimum (determined by VOCs/ NO_x ratio). The level of NO_2 which represents a major part of NO_x is critical for determining the O_3 production efficiency through the formation of $O(^3P)$ atom. Subsequently, $O(^3P)$ combines with molecular oxygen (O_2) leading to the formation of O_3 . On the other hand, excessive conversion of NO from NO_2 can directly react with O_3 , leading to loss of ambient O_3 by the following titration reaction.

Reaction set 2



In addition to the direct effect of UV radiation on O_3 production, emissions of some O_3 precursors are temperature-dependent and peak during the mid-summer in the tropical region. For example, the biogenic or natural emissions of hydrocarbons are particularly sensitive to temperature and follow the seasonal cycles of controlling

*For correspondence. (e-mail: lokesh@prl.res.in)